

Héloïse Beaugendre¹

François Morency²

Wagdi G. Habashi³
Director

Computational Fluid Dynamics Laboratory,
Department of Mechanical Engineering,
McGill University,
688 Sherbrooke Street West, 7th Floor,
Montréal, Québec H3A 2S6 Canada

Development of a Second Generation In-Flight Icing Simulation Code

Two-dimensional and quasi-3D in-flight ice accretion simulation codes have been widely used by the aerospace industry for the last two decades as an aid to the certification process. The present paper proposes an efficient numerical method for calculating ice shapes on simple or complex 3D geometries. The resulting ice simulation system, FENSAP-ICE, is built in a modular fashion to successively solve each flow, impingement and accretion via field models based on partial differential equations (PDEs). The FENSAP-ICE system results are compared to other numerical and experimental results on 2D and slightly complex 3D geometries. It is concluded that FENSAP-ICE gives results in agreement with other code calculation results, for the geometries available in the open literature. [DOI: 10.1115/1.2169807]

Introduction

Not all certification conditions can be ice tunnel-tested, flight-tested, tanker-tested or encountered in natural icing testing. The certification process usually consists of a mix of experimental and numerical methods that make it possible to explore, safely, the entire combined aerodynamic and icing envelopes. For more than 50 years now, the aircraft icing community has been using analytical methods to calculate impingement limits and predict ice shapes to be subsequently attached to an aircraft for flight-testing [1]. The decrease in computer calculation cost has led to the rapid development of ice accretion simulation tools in the early 1980s [2]. Usually, such methods are based on either a 2D or quasi-3D inviscid flow code (Panel method) to compute the airflow solution, on Lagrangian particle tracking techniques for droplet impingement calculations, and on a 1D mass and heat transfer balance at the surface to predict ice shapes. The best-known codes using this structure are NASA's LEWICE [3], ONERA [4], TRAJICE2 [5], and Bombardier Aerospace's CANICE [6].

Although code structure has remained mostly the same for nearly 20 years, several improvements have been proposed, making it possible for the most advanced codes to tackle 3D problems [7]. One of the advantages of these pioneering methods is their fast calculation speed, especially on 2D problems. They have, however, known limitations, the most obvious being the inability to handle flow with separation. It is well known that viscous/nonviscous coupling methods are difficult to apply to separated flow, more the norm than the exception for most of the glaze ice accretion cases.

Current computational fluid dynamics technologies can overcome some of the limitations of these fully mature methods, and open new possible uses for in-flight icing prediction tools. Advanced notions such as using computational fluid dynamics to couple aerodynamics and icing, of using computational fluid dynamics to assess the stability and control of iced aircraft or for building a database for an in-flight icing simulator can then be contemplated.

The FENSAP-ICE approach views icing accretion simulation as the interlinking of:

- The computation of the clean and degraded flows via a 3D compressible turbulent Navier-Stokes equations (by any computational fluid dynamics code; here with FENSAP [8]: Finite Element Navier-Stokes Analysis Package);
- The computation of the collection efficiency by a 3D Eulerian method (here with DROP3D [9]);
- The solution of 3D mass balance and heat transfer at surface, using partial differential equations, for prediction of 3D ice accretion shapes (here with ICE3D [10]);
- A conjugate heat transfer problem, in the presence of an anti-icing heat flux across the wing skin (for example, with the use of CHT3D [11]);

all four approaches being partial differential equations (PDE)-based. As shown in Fig. 1, the modules are set in an interactive loop.

This paper first presents a short description of the first three modules. The code results are compared to other 2D and quasi-3D numerical and experimental results from NASA, and are demonstrated for ice accretion on a 3D rotor blade tip.

FENSAP-ICE's Modules Description

Airflow solver. The airflow solver of FENSAP-ICE, FENSAP, can act in an inviscid (Euler) or viscous (Navier-Stokes) mode, as necessitated by the application at hand. For ice accretion simulation, results are extremely sensitive to the turbulent heat fluxes at walls and the Navier-Stokes equations, with appropriate turbulence models, are called for. Currently, a one-equation turbulence model (Spalart-Allmaras [12]), including extension for rough-wall treatment [13], has been implemented and successfully validated [14]. The validation has been done against experimental and numerical results on an attached flow with known equivalent sandgrain roughness value. Glaze ice accretion simulation results depend on the roughness value selected, and an empirical correlation relating roughness to velocity, liquid water content and static temperature, developed for LEWICE, is used [14,15].

The Spalart-Allmaras model offers the possibility to locally trip the flow if the transition point location is known. For ice accretion calculation, the transition location is not known and the flow is assumed to be fully turbulent. Thus, it is expected that numerical results overpredict heat flux near the stagnation point, where the flow should be laminar. But, as ice starts to accrete on an airfoil,

¹Presently at: MAB, Bureau 281, Université Bordeaux I, 351, Cours de la Libération, 33405 Talence Cedex, France.

²Presently at: Département de Génie Mécanique, École de Technologie Supérieure, 1100 Rue Notre-Dame Ouest, Montréal, Québec, H3C 1K3, Canada.

³Corresponding author.

Contributed by the Fluids Engineering Division of ASME for publication in the JOURNAL OF FLUIDS ENGINEERING. Manuscript received April 28, 2004; final manuscript received February 24, 2005. Review conducted by Joseph Katz.

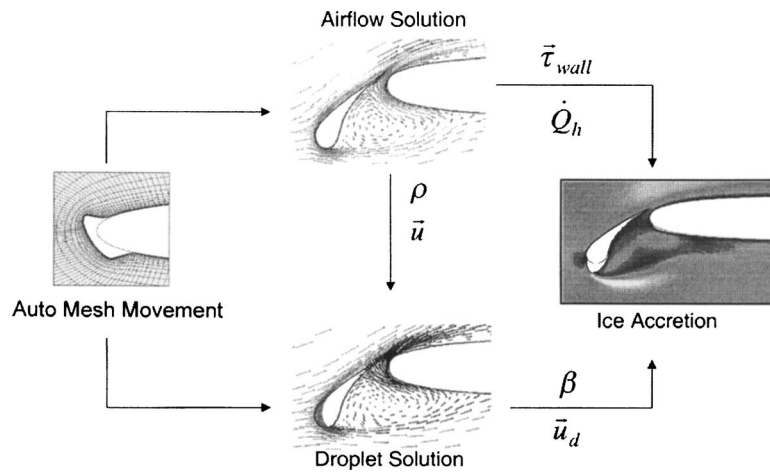


Fig. 1 Module interactions within FENSAP-ICE

ice roughness in the stagnation point area causes perturbations in the boundary layer. Transition from laminar to turbulent flow occurs earlier than for a clean airfoil, in the near vicinity of the stagnation point.

Spatial discretization is carried out by finite element method and the nonlinear governing equations are linearized by a Newton method. To advance the solution in time, an implicit Gear scheme is used, along with a generalized minimum residual (GMRES) procedure to iteratively solve the resulting linear equations matrix system. In order to have a nearly optimal mesh for a required number of nodes for a Navier-Stokes calculation, an automatic anisotropic mesh optimization procedure is used [16]. This technology has been shown to yield user-independent and solver-independent results as long as one is not limited in mesh size. When computer memory constrains the problem size, then mesh adaptation provides a rapid way to generate meshes that optimize the prediction of a known scalar physical property of the flow, most often the Mach number.

Gradients needed for heat fluxes at walls are also accurately calculated via a consistent finite volume method postprocessing approach developed by Gresho et al. [17]. This method substantially reduces the numerical error in flux evaluation. Good results will be obtained if the physical models, including heat fluxes and the turbulence model, are appropriate for the problem. It is generally admitted that one- and two-equation turbulence models have difficulties to accurately predict the flow field in a separated region, such as the flow behind an ice horn or ridge, but potential flow methods completely fail in these cases.

Droplet flow solver. The Eulerian droplet impingement model is essentially a two-fluid model consisting of the Euler (inviscid) or Navier-Stokes (viscous turbulent) set of equations for dry air, augmented by the following droplet-specific continuity and momentum equations:

$$\frac{\partial \alpha}{\partial t} + \nabla \cdot (\alpha \mathbf{u}_d) = 0 \quad (1)$$

$$\frac{D\mathbf{u}_d}{Dt} = \frac{C_D \text{Re}_d}{24K} (\mathbf{u}_a - \mathbf{u}_d) + \left(1 - \frac{\rho_a}{\rho_w}\right) \frac{1}{\text{Fr}^2} \mathbf{g} + \frac{\rho_a}{\rho_w} \frac{D\mathbf{u}_a}{Dt} \quad (2)$$

where the variables α and \mathbf{u}_d are mean values, respectively, of the nondimensional water volume fraction and droplet velocity over a small fluid element around the location x at time t . The first term on the right-hand side of Eq. (2) represents the drag force on the droplets, while the second and third terms represent, respectively, the buoyancy force from gravity and the forces exerted on an air particle that would have occupied the volume of the droplet [18]. In most cases, the third term is negligible due to the low ratio of

air to water densities.

An empirical correlation is used for the drag coefficient, C_D . The two-fluid model assumes spherical monodispersed droplets, at the median volumetric diameter of the sample size distribution. The spherical droplet approximation is valid for droplet Reynolds numbers below 500. No collision or mixing between the droplets is accounted for, as these are not significant in certification icing situations. The following empirical equation gives the drag coefficient around a sphere, as a function of the Reynolds number:

$$C_D = (24/\text{Re}_d)(1 + 0.15 \text{Re}_d^{0.687}) \quad \text{for } \text{Re}_d \leq 1300 \quad (3)$$

$$C_D = 0.4 \quad \text{for } \text{Re}_d > 1300$$

The correlation used goes above $\text{Re}_d=500$ because during the iterative convergence of the numerical solution, higher droplet Reynolds numbers may occur. The final converged solution, however, should not contain local droplet Reynolds numbers above 500. Otherwise, it means that a different correlation accounting for droplet deformation must be used.

The nondimensional air velocity, \mathbf{u}_a , is obtained from the solution of the Navier-Stokes equations. Because of the low liquid water concentration, the effect of the droplets on the airflow is neglected. Airflow can thus be determined before solving Eqs. (1) and (2).

A finite element Galerkin formulation is used to discretize the set of Eqs. (1) and (2), with a streamline upwinding Petrov-Galerkin (SUPG) term added [19].

Ice Accretion Solver

The 3D partial-differential equation-based equilibrium model introduced in Ref. [20] is derived based on the Messinger [1] model. It has been further improved to predict the ice accretion and water runback on the surface [10]. The velocity \mathbf{u}_f of the water in the film is a function of coordinates $\mathbf{x}=(x_1, x_2)$ on the surface and y normal to the surface.

A simplifying assumption consists of taking a linear profile for $\mathbf{u}_f(\mathbf{x}, y)$, with a zero velocity imposed at the wall, i.e.,

$$\mathbf{u}_f(\mathbf{x}, y) = \frac{y}{\mu_w} \tau_{\text{wall}}(\mathbf{x}) \quad (4)$$

where τ_{wall} , the shear stress from the air, is the main driving force for the water film. By selecting a linear velocity profile, body forces such as pressure and gravity are neglected. Except perhaps near stagnation lines, body forces can be shown to have negligible effect on the thin water films that occur in the case of ice accretion [15].

By averaging across the thickness of the film, a mean water film velocity is obtained

$$\bar{\mathbf{u}}_f(\mathbf{x}) = \frac{1}{h_f} \int_0^{h_f} \mathbf{u}_f(\mathbf{x}, y) dy = \frac{h_f}{2\mu_w} \tau_{\text{wall}}(\mathbf{x}) \quad (5)$$

The resulting system of partial differential equations is thus the following mass conservation and energy conservation equations,

$$\rho_w \left[\frac{\partial h_f}{\partial t} + \text{div}(\bar{\mathbf{u}}_f h_f) \right] = U_\infty \text{LWC} \beta - \dot{m}_{\text{evap}} - \dot{m}_{\text{ice}} \quad (6)$$

where the three terms on the right-hand side correspond to the mass transfer by water droplet impingement (source for the film), the evaporation and the ice accretion (sinks for the film), respectively,

$$\begin{aligned} \rho_w \left[\frac{\partial h_f C_w T}{\partial t} + \text{div}(\bar{\mathbf{u}}_f h_f C_w T) \right] = & \left[C_w T_{d,\infty} + \frac{\|\mathbf{u}_d\|^2}{2} \right] \times U_\infty \text{LWC} \beta \\ & - 0.5(L_{\text{evap}} + L_{\text{subl}}) \dot{m}_{\text{evap}} \\ & + (L_{\text{fusion}} - C_{\text{ice}} T) \dot{m}_{\text{ice}} + \epsilon \sigma (T_\infty + 273.15)^4 \\ & - (T + 273.15)^4 + \dot{Q}_h \end{aligned} \quad (7)$$

where the first three terms on the right-hand side, correspond, respectively to the heat transfer caused by the supercooled water droplets impinging on the surface, and that from evaporation and ice accretion. The last two terms in the equation represent the radiative and convective heat transfer.

The convective heat transfer is obtained from the computational fluid dynamics code, by imposing a constant clean airfoil surface temperature above the free-stream temperature. The heat flux is converted into a heat transfer coefficient, before ice accretion calculations, because the heat transfer coefficient depends only weakly on the surface temperature distribution [21].

The coefficients ρ_w , C_w , C_{ice} , L_{evap} , L_{subl} , L_{fusion} represent physical properties of water, while $T_{d,\infty}$, U_∞ , LWC , and T_∞ are airflow and droplet parameters specified by the user. The ambient icing conditions completely determine those values. The temperatures are in Celsius.

The Eulerian droplet module provides local values for the collection efficiency β and the droplet impact velocity \mathbf{u}_d . The flow solver provides the local wall shear stress τ_{wall} and the convective heat flux \dot{Q}_h . The evaporative mass flux is recovered from the convective heat flux using a parametric model [6]. There remain three unknowns: the film thickness h_f , the equilibrium temperature T within the air/water film/ice/wall interface, and the instantaneous mass accumulation of ice \dot{m}_{ice} . Compatibility relations are needed to close the system and one way to write them is the following:

$$h_f \geq 0 \quad (8)$$

$$\dot{m}_{\text{ice}} \geq 0 \quad (9)$$

$$h_f T \geq 0 \quad (10)$$

$$\dot{m}_{\text{ice}} T \leq 0 \quad (11)$$

The discretization of these equations is via finite volume method. The trace of the three-dimensional mesh at the air-structure/ice shape interface is called the surface mesh. From the surface mesh, a dual surface mesh is obtained by connecting the centroids of the surface mesh cells to the mid-edges of the cells. The unknowns are then computed at the center of each cell, corresponding one-to-one to the nodes of the finite element method used for the air and droplet solutions.

After a given ice accretion time, the ice accretion solver returns a wall temperature distribution and the displacements of the sur-

Table 1 Ambient conditions corresponding to 2D test cases

Parameter	Run 403	Run 404	Run 308
T_∞	262.04 K	256.49 K	262.04 K
P_∞	100 kPa	90.76 kPa	90.76 kPa
U_∞	102.8 m s ⁻¹	102.8 m s ⁻¹	102.8 m s ⁻¹
AoA	4 deg	4 deg	4 deg
MVD	20 μm	20 μm	20 μm
LWC	0.55 g/m ³	0.55 g/m ³	1 g/m ³
Re_∞	4.39×10^6	4.14×10^6	4.14×10^6

face nodes. These displacements and temperature distribution can be used to calculate a new airflow solution and start a new calculation cycle. With a Navier-Stokes flow solver, for sufficiently large ice horns, separation may occur. This separation will affect the overall flow field and the local heat transfer coefficient. Although actual turbulence models are not very accurate for separated flows, they still represent a significant improvement on a viscous/nonviscous coupling method. Knowing that first generation codes fail to predict this separation, it can thus be expected that even for 2D glaze ice cases, discrepancies will exist between numerical results.

In the three-dimensional cases, ice accretion results were obtained using only one cycle of calculation (one-shot ice accretion). Thus, the effect of ice accretion on the airflow and droplets fields is neglected. It means losing part of the advantage of using a Navier-Stokes solver. For the actual 3D test cases, this simplification is justified by the rime ice accretion conditions that produce ice shapes with relatively low impact on airflow for the rotor blade tip. This will have to be confirmed in the future by running multiple layer ice accretions.

To do multilayer ice accretions in 3D would take a large amount of computing time. Also, considering that for the nacelle only one-shot ice accretion results are available from the LEWICE code, in this article only one-shot results are shown for 3D calculations.

Two-Dimensional Validations

ICE3D has been compared to numerical solutions obtained with LEWICE, and experimental results obtained in the NASA Glenn Icing Research Tunnel (IRT) [22]. All FENSAP 2D calculations are carried out in a pseudo-3D manner on meshes of one element thickness in the spanwise direction. A consensus [23,24] about the comparison criteria of two icing shapes is difficult to obtain. Indeed, the focus can be on different criteria such as the limit of impact, the ice thickness or the location and angle of a possible horn, etc. As a consequence, the comparisons remain most of the time subjective but conservative enough to satisfy aircraft safety requirements.

Mesh density effects. The effect, on the ice accretion simulation, of mesh density around the leading edge of a NACA 0012 airfoil has been studied with a coarse (90 mesh points on the airfoil), medium (180 mesh points), and fine grid (360 mesh points). The meshes contain, respectively, a total of 23,350, 36,130, and 61,690 nodes. The spacing in the direction normal to the wall is kept the same for the 3 meshes and is equal to $8.4 \times 10^{-6} c$, c being the chord of the airfoil. The ambient conditions selected for this test case correspond to the LEWICE Run 403 [22] and are given in Table 1. The accretion time is 7 min. The airflow, impingement and ice accretion solutions on the 3 meshes are compared to each other and compared to LEWICE solutions. For the airflow and impingement solutions the results are plotted against the distance from the stagnation point.

Airflow solution. The turbulence model selected for the simulation is the one-equation Spalart-Allmaras model with an equiva-

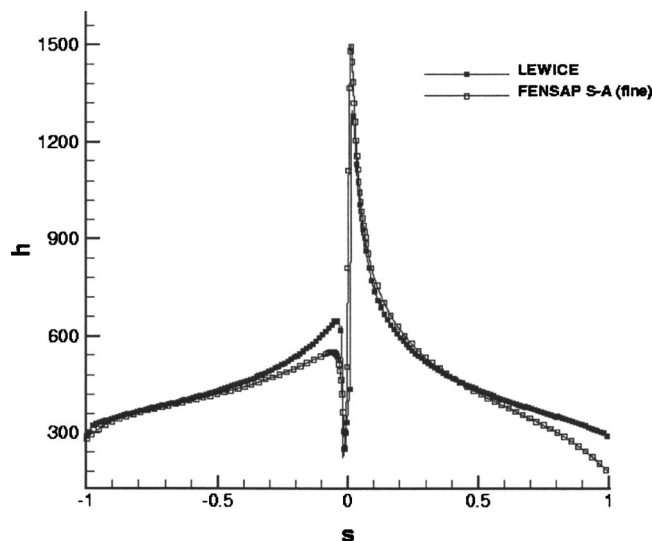


Fig. 2 Convective heat transfer coefficient distribution against the distance from stagnation point

lent sandgrain roughness of 0.55 mm. The grid study shows that the solutions on the medium and fine grids are similar and appear to be mesh-independent, as far as the heat transfer coefficient is concerned.

LEWICE uses an integral method to solve the boundary layer. LEWICE and FENSAP solutions are compared in Fig. 2. The differences between the two curves close to the trailing edge are due to the boundary layer thickness, not taken into account in the LEWICE code. Close to transition points the differences are most probably induced by the turbulence model. The equivalent sandgrain roughness coefficient used for this calculation is the same as in LEWICE. This roughness coefficient is especially calibrated for LEWICE. Although the two turbulence models employed are strongly different, the two solutions agree pretty much and the results are satisfactory.

Impingement solution. The local collection efficiency curves are identical for the three meshes, thus droplet solutions appear to be mesh-independent.

The comparison with LEWICE is shown in Fig. 3. The maxi-

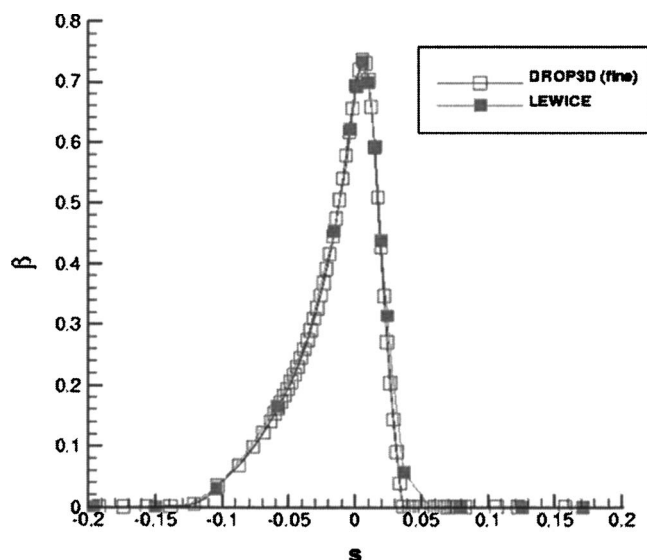


Fig. 3 Local collection efficiency distribution against the distance from stagnation point

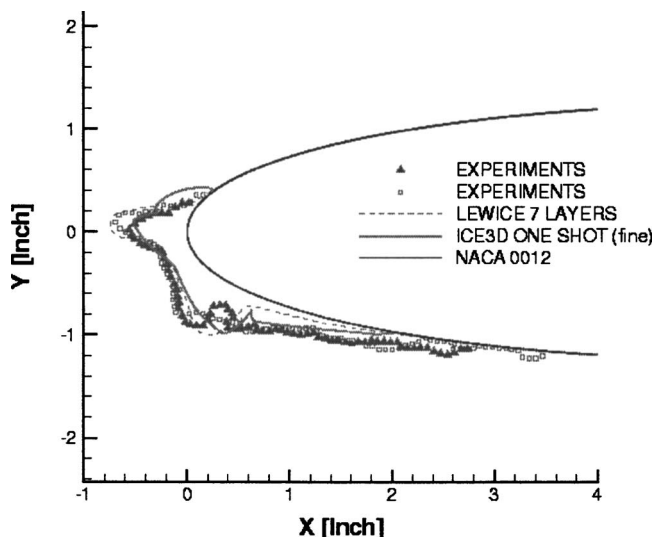


Fig. 4 Run 403 [NASA-CDROM], ice shape comparison between ICE3D (fine grid), LEWICE and experiments

mum collection efficiency predicted by the two codes is identical. The impingement limits are slightly different on the upper part of the airfoil ($s \geq 0$). This is most probably due to a small difference in flow fields. LEWICE solves for a potential flow and the angle of attack is lowered from 4 deg to 3.5 deg to match the overall lift coefficient. For the Navier-Stokes numerical solution, a free stream angle of attack of 4 deg is used.

Ice accretion solution. For the ice accretion module, a one-shot ice accretion simulation is performed on each mesh. The aim is to have larger ice shapes to compare, and also not to mix the effect of mesh density with the effect of airflow solution updates on the solution. Beaugendre [15] has studied this last aspect.

The comparison of ice shapes on the three meshes shows not much difference, and only results on the finer mesh are shown. The mass of ice accreted is the same for the three meshes and is equal to 0.496 kg per unit span.

For this run, two experimental solutions are available and plotted in Fig. 4. The LEWICE numerical solutions obtained with a multisteping approach composed of 7 layers is also available and shown. The one-shot ICE3D shape is acceptable compared to the experimental and numerical solutions, especially if we take into account the fact that the over predicted ice thickness on top of the airfoil will substantially decrease if a multisteping approach were used. Indeed, this part of the airfoil will be in the shadow zone of the bump located between the coordinates: $0 < Y < 0.2$ in.

Validation on Airfoil: NACA 0012. The NACA 0012 airfoil has been used in several test entries. The data from this airfoil represent the highest number of ice shapes that have been created in the icing research tunnel. Through all this section, the ice shapes are plotted in inches.

Run 404. In the first comparison, ice is accreted for 7 min on a NACA 0012 airfoil at 4 deg angle of attack. The ambient icing conditions, which should be close to rime ice accretion are given in Table 1 and correspond to LEWICE Run 404 [22].

Figure 5 shows the final ice shape computed by LEWICE and ICE3D, compared to the experimental ice shape obtained in the IRT. The limits of impact are identical for LEWICE and ICE3D and match the experiments on the suction side of the airfoil, but are underpredicted by both codes on the pressure side of the airfoil. ICE3D's ice shape is thicker and closer to the experimental ice shape than LEWICE on the upper part of the airfoil. This may be due to a larger estimation of the water evaporation by

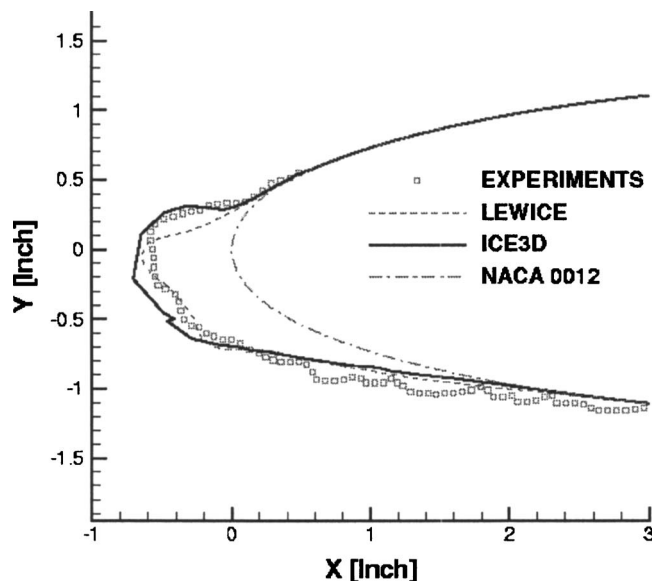


Fig. 5 Run 404 [NASA CD-ROM], ice shape comparison between ICE3D, LEWICE, and experiments

LEWICE. ICE3D also predicts a slightly smaller ice thickness on the pressure side, where the LEWICE solution is closer to the measurement.

Run 308. In the second comparison, ice is accreted on a NACA 0012 airfoil at a 4 deg angle of attack for 231 s. The ambient conditions, closer to glaze ice conditions, are summarized in Table 1 and correspond to LEWICE Run 308 [22].

Figure 6 shows the comparison between LEWICE and ICE3D numerical solutions after 47.58 and 95.16 s of accretion. At 47.58 s of accretion, ICE3D and LEWICE solutions are identical: same ice thickness and limits of impact for both codes. After 95.16 s of accretion, LEWICE and ICE3D solutions remain very close to each other, LEWICE predicting a slightly bigger amount of runback than ICE3D. Both codes predict the formation of a horn on the upper part of the NACA 0012 airfoil, with the same

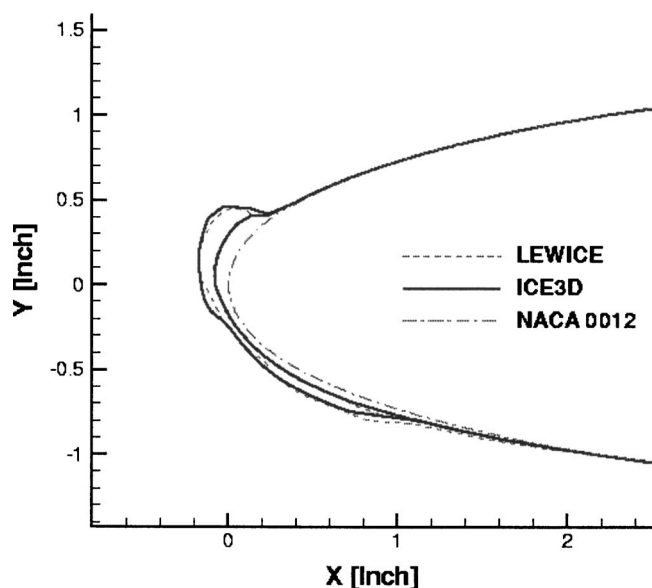


Fig. 6 Run 308 [NASA CD-ROM] comparison between ICE3D and LEWICE after 47.58 and 95.16 s of ice accretion

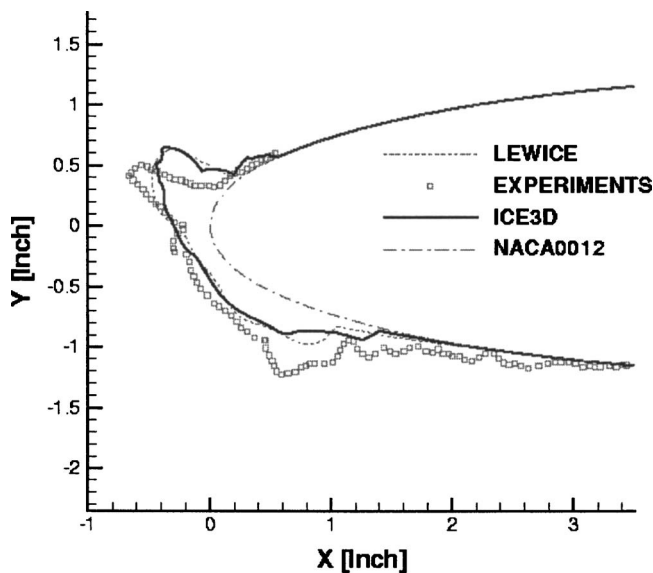


Fig. 7 Run 308 [NASA CD-ROM] comparison between ICE3D, LEWICE and IRT experimental ice shape

angle and ice thickness.

After 95.16 s of accretion, the horn predicted by ICE3D induces a separation in the flow solution. Contrary to LEWICE, which may be able to predict but not compute separation with only a viscous/inviscid interaction, ICE3D's convective heat transfer coefficient and shear stress decrease suddenly in the separation area. As a consequence, impact may be predicted behind a horn as can be seen in Fig. 7. ICE3D's final ice shape is very close to LEWICE's, but both codes fail to predict the horn's angle of the experimental ice shape. There is still room for improvement in the quality of ice-accretion-shape predictions yielded by current icing codes, as large differences between predicted and experimental ice shapes are often encountered [24] in glaze ice conditions, compounded by the problem of the lack of consistency of ice shapes produced in icing wind tunnels.

3D Helicopter Rotor Blade Tip Results

The first test case considered is a three-dimensional helicopter rotor blade tip. This case was selected because of the availability of experimental and numerical results. Its three-dimensional effects are small, and a quasi-three-dimensional model that accretes ice along the flow streamlines from ONERA calculated a numerical solution [4] to compare to.

This three-dimensional helicopter rotor tip geometry is rather briefly described in paper [4] as follows:

"...from the base to the top along the span, the chord varies from 0.6 to 0.2 m, the leading edge sweep angle starts at 0 and ends at 60 deg. The trailing edge is perpendicular to the flow and is lightly spun so that the incidence angle at the top is 0.74 deg less than at the base. The span is 0.48 m. The rotor blade tip is built from a NACA 13106 airfoil."

Based on this short description, a computer aided design (CAD) of the geometry was produced with the ICEM DDN software. The one-equation Spalart-Allmaras model was used for turbulence modeling and mesh adaptation was carried out with OptiMesh [25], an anisotropic (highly directional and highly stretched) automatic mesh adaptation code. Unfortunately, it turns out that the experimental model does not follow exactly the description given in paper [4].

Airflow solution and mesh adaptation. The conditions for the simulation are shown in Table 2.

To improve the quality of the flow solution, three mesh adap-

Table 2 Ambient conditions for the helicopter rotor blade tip simulation

Parameter	Value
T_{∞}	-30.5°C
P_{∞}	456 h Pa
Mach	0.52
AoA	9.5 deg
MVD	20 μm
LWC	1 g/m ³
time	91 s

tations cycles were carried out with OptiMesh. The OptiMesh algorithm has an a posteriori error estimate based on the Hessian of the solution (hence proportional to the truncation error) and then uses mesh movement, edge refinement, coarsening, and swapping to automatically yield a nearly-optimal adapted grid. These actions are done throughout the numerical solution and the grid edges migrate where the flow phenomena mandate. OptiMesh has proven to asymptotically get to a unique final grid [26], no matter what the initial grid is like and yields results independent of the code used. The initial mesh has 221,800 nodes and 1,118,131 elements, and the final adapted one has 467,705 nodes and 2,546,857 elements.

The grid convergence index method suggested by Roache [27] for unstructured grid refinement based on the number of nodes is used to get an idea of the accuracy of the pressure coefficient distribution on the wing. Accuracy of the C_p distribution at the four stations defined below is conservatively estimated around 4%. Although this error seems large, it was judged acceptable considering that the goal is to predict ice shape using a one-shot ice accretion, thus neglecting effects of the ice growth on the airflow and droplet solutions.

An equivalent sandgrain roughness was used for the icing calculations and it is obtained using an empirical correlation given in [3], and corresponds to 0.269 mm in this case.

To help result discussion, 2D cuts at four different span wise locations are performed. Each cut corresponds to a plane (x, z), and the cuts are referred to as station 1 (location $y=0.09$ m), station 2 (location $y=0.25$ m), station 3 ($y=0.30$ m), and station 4

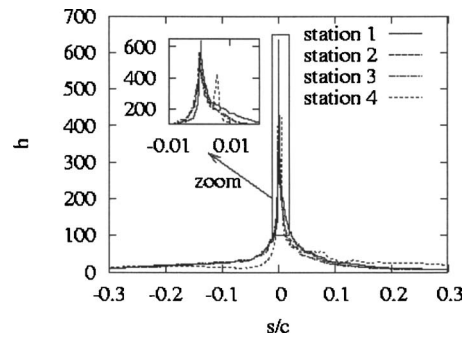


Fig. 9 2D cuts of the convective heat transfer coefficient, in W/m² K

($y=0.45$ m). The origin of the coordinate system is at the root of the wing at the leading edge. The y -axis is in the spanwise direction, and the x -axis is the curvilinear distance along the surface in the chord wise direction. Positive values for x -axis are above the plane $y=0$, and negative value below. The chord at the root of the wing, namely 0.586 m, scales the curvilinear distance.

As presented in Fig. 8, the finite blade modeled in this article engenders 3D aerodynamic effects; first, with the creation of a local aerodynamic angle of attack different from the free stream and, second, with the creation of a tip vortex at the blade extremity. Due to a negative twist angle, a separation bubble appears in that region. All aerodynamic variables are affected by this flow pattern.

Figure 9 shows the convective heat transfer coefficient for stations 1, 2, 3, and 4. The heat transfer coefficient curves are quite similar along the blade, except close to the tip, station 4, where the vortex induces separation. At this station, the heat transfer coefficient decreases rapidly on the upper side of the wing, before increasing abruptly at the reattachment point. In a separation bubble, heat transfer coefficients are expected to be small.

Collection efficiency distribution. In Fig. 10, the coordinates along the airfoil section corresponding to each station are divided, using the root chord length, to make comparison easier. Keeping in mind that the wing section reduces in size from the root to the

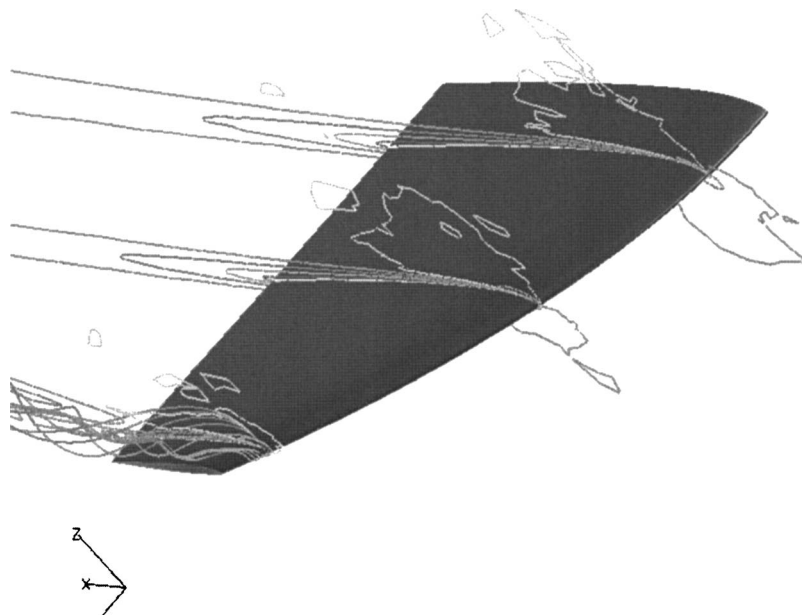


Fig. 8 Turbulent airflow solution, Mach number contours, streamlines at the tip and C_p distribution on the blade

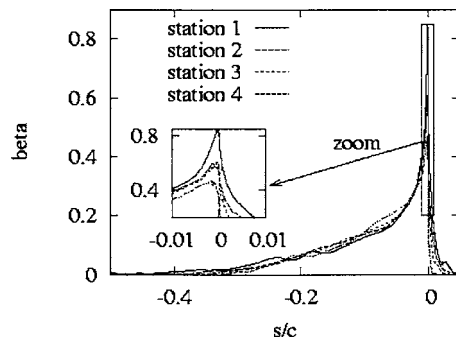


Fig. 10 2D cuts of the collection efficiency for stations 1, 2, 3, and 4 along the curvilinear coordinate

tip, even if the impingement limits on the lower side are almost constant, they extend further back on the airfoil closer to the tip. On the other hand, the impingement limit on the upper side of the blade decreases from station 1 to station 4. This effect is due to the negative twist angle.

Ice accretion. Once the FENSAP airflow solution and the collection efficiency from DROP3D have been determined, ice accretion can be performed, using ICE3D, on the adapted grid. The 91-s exposure has been simulated in one shot. Figure 11 gives a 3D view of the rime ice accretion at tip.

Two-dimensional cuts of the ice shape corresponding to stations 1, 2, 3, and 4 are plotted in Fig. 12. The global aspect of the ice shape qualitatively agrees with the numerical and experimental results of ONERA [4], keeping in mind that the ONERA results were obtained on a slightly different geometry. The 3D effects are not spectacular, as the geometry does not present strong 3D features and the very cold temperature corresponds to rime ice conditions, making water runback not an important factor. In fact, the ice shape mostly depends on impingement, and this is a good test case to ascertain values calculated by DROP3D.

3D Nonaxisymmetric Nacelle

In this calculation the aim is to predict ice accretion on a 3D nonaxisymmetric Boeing 737-300 [28] nacelle inlet. A complete set of computational and experimental results, made by NASA [29], are available for the airflow solution and the collection efficiency, but not for the ice shapes. Thus, the only thing that one can do is compare ICE3D's predictions to LEWICE's.

The icing calculation process requires three steps: the computation of the airflow, the computation of the droplet solution, and the prediction of the ice shape. Each "step solution" will be compared to the corresponding LEWICE solution and to the experiments, if available.

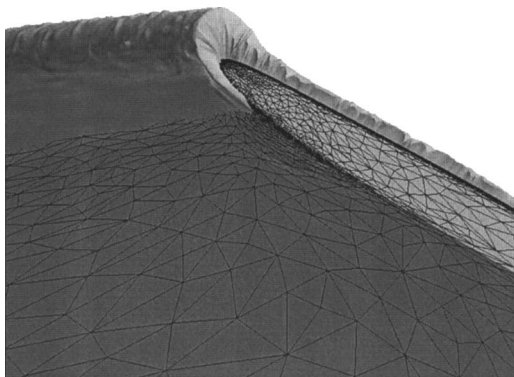


Fig. 11 3D ice shape at blade tip

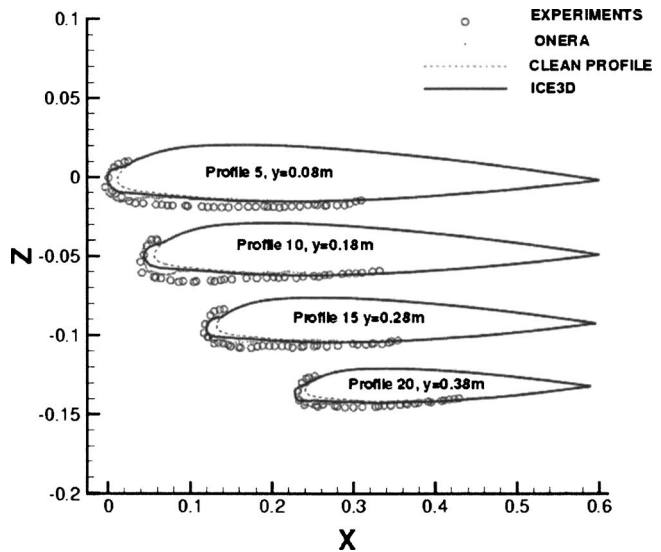


Fig. 12 2D ice cuts along the span wise direction for stations 1, 2, 3, and 4

Two cases were analyzed at a true airspeed of 75 m/s, an inlet mass flow of 10.4 kg/s, a static pressure of 95840 Pa, a droplet Mean Volumetric Diameter of 20.36 μm , and nacelle incidences of 0 deg (run id 092385-1,2,3-737-0 in Ref. [28]) and 15 deg (run id 092385-13,14,15-737-15 in Ref. [28]). 3D rime ice accretion result is shown in Fig. 13 for the 15 deg case.

Tran et al. [30] used OptiMesh and compared Mach number distributions along circumferential cuts, for both incidences. The starting mesh had 108,000 nodes and 624,000 tetrahedra. After two adaptation cycles, the mesh size increased to 152,000 nodes and 824,000 highly anisotropic tetrahedral elements. The calculated Mach number distributions are in good agreement with both experimental and LEWICE results for all circumferential positions, at both incidences. A sample of results, postprocessed to be in the same units of those of Ref. [28], is shown in Figs. 14 and 15.

In order to compute the local catch efficiency β , DROP3D was run for a Langmuir-D droplet distribution. The comparison of local catch efficiency distribution along the same circumferential cuts is presented in the same article [30]. The peak is shown to be within experimental repeatability, estimated to be between 0.20 and 0.25[30]. The results show that, FENSAP-ICE and LEWICE catch efficiency results agree over most of the nacelle. However,

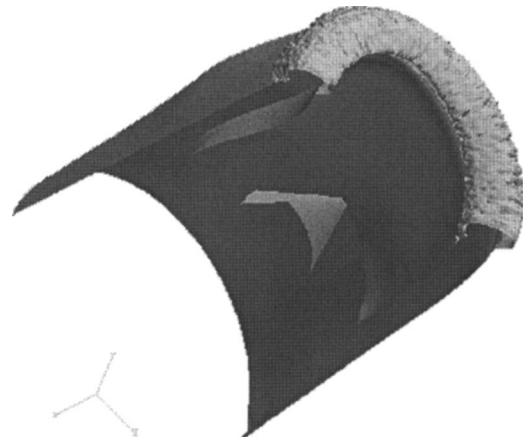


Fig. 13 3D ice accretion on the Boeing 737-300 inlet, rime ice accretion for 15 deg AoA and an inlet mass flow of 10.4 kg/s

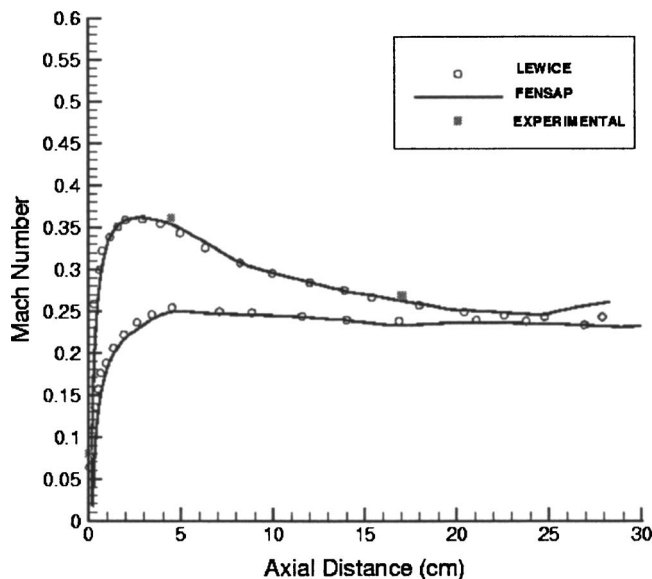


Fig. 14 Mach number distribution for the Boeing 737-300 inlet for 0 deg AoA and an inlet mass flow of 10.4 kg/s, comparison between FENSAP, LEWICE and Experiments, circumferential cut at 45 deg

the impingement limits predicted by FENSAP-ICE are somewhat closer to the experimental values, as it uses a computational fluid dynamics (field) approach that has no difficulties near boundaries. Figures 16 and 17 present selected comparisons between DROP3D, LEWICE, and the experiments.

Two icing conditions were calculated for each incidence of the Boeing 737-300 inlet. The conditions were chosen to represent a rime and a glaze ice situation. The rime conditions are the following: an accretion time of 30 min with a LWC of 0.2 g/m^3 and a static temperature of -29.9°C . For the mixed or glaze ice conditions, the time of exposure is still 30 min but the LWC is 0.695 g/m^3 and the static temperature is -9.3°C .

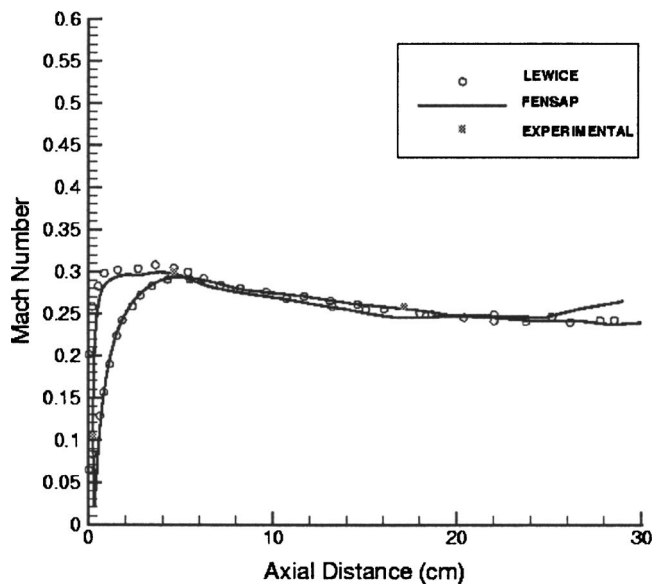


Fig. 15 Mach number distribution for the Boeing 737-300 inlet for 15 deg AoA and an inlet mass flow of 10.4 kg/s, comparison between FENSAP, LEWICE and Experiments, circumferential cut at 45 deg

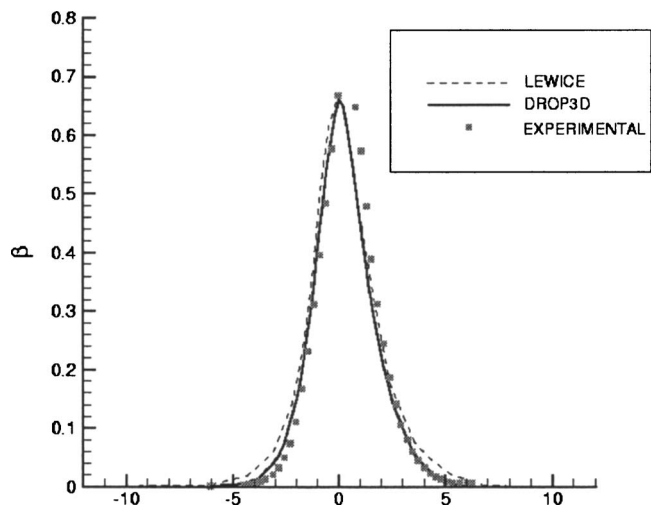


Fig. 16 Local collection efficiency distribution for 0 deg AoA, comparison between DROP3D, LEWICE and Experiments, circumferential cut at 180 deg

In the rime ice case, the comparison between LEWICE and ICE3D is very good for all circumferential positions for both incidences, Figs. 18 and 19.

For the glaze ice condition, the LEWICE and ICE3D predicted ice shapes, Figs. 20 and 21, agree pretty well for all circumferential positions and for both incidences.

Although no experimental data were available, it is comforting that the results obtained by the two codes are in good agreement and look consistent with the conditions for which the shapes were generated and with the airflow and droplet solutions.

Conclusions

A second-generation numerical approach based on partial differential equations has been proposed for calculating all aspects of in-flight icing on complete aircraft. FENSAP-ICE, a code based on the proposed method, has been used to calculate ice shapes on 2D airfoils and 3D aircraft parts. Comparisons against 2D experimental and numerical results available in the literature show that the FENSAP-ICE code gives results as accurate as first generation

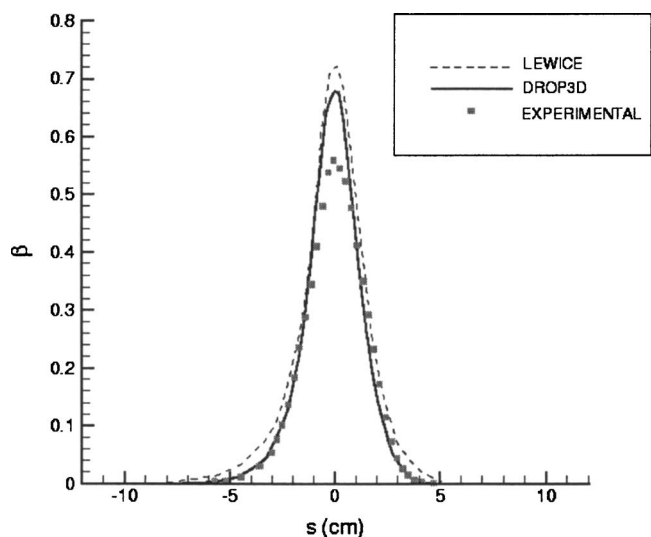


Fig. 17 Local collection efficiency distribution for 15 deg AoA, comparison between DROP3D, LEWICE and Experiments, circumferential cut at 90 deg

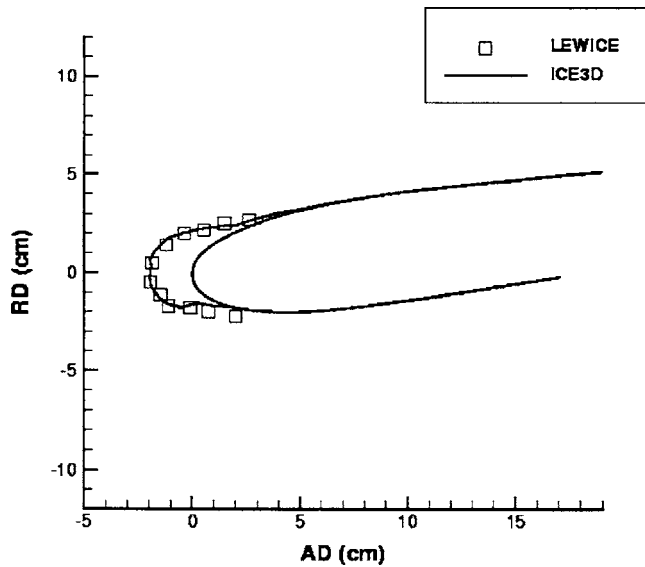


Fig. 18 Rime ice for the Boeing 737-300 inlet for 0 deg AoA, comparison of analytical ice shapes between ICE3D and LEWICE, circumferential cut at 45 deg

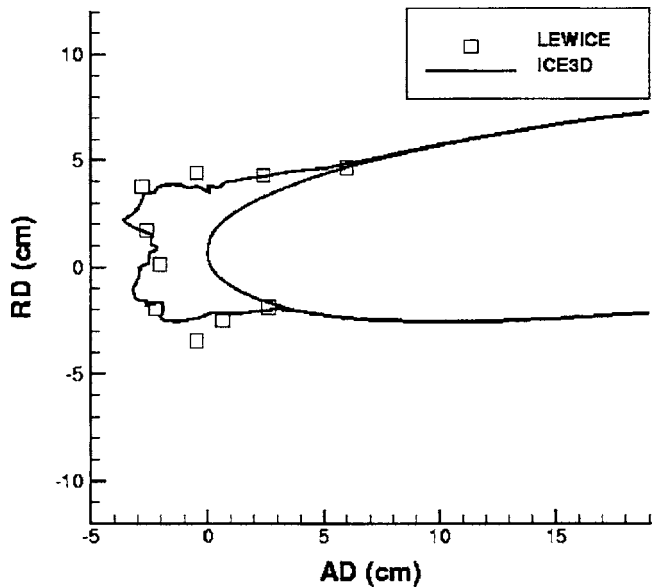


Fig. 20 Glaze ice for the Boeing 737-300 inlet for 0 deg AoA, comparison of analytical ice shapes between ICE3D and LEWICE, circumferential cut at 135 deg

icing codes. Now that the numerical scheme has been shown to work, more tests will have to be carried out in order to test the limits of the physical model used. For example, capability of the turbulence model to predict correctly the separated area behind an ice horn will have to be verified. Also, the effect of the separation area on the growing ice shape is not yet clear. The main strength of the new method compared to first generation icing codes, apart from the 3D ice prediction capability, is the possibility to use advances from other computational fluid dynamic areas where partial differential equations are used.

Apart from the modeling inaccuracies related to the turbulence model on rough surfaces and in separated areas, there are other possible sources of numerical error: mesh related error during solution and error on collection efficiency coefficients due to the lack of updating of the air solution. Using mesh adaptation based on airflow solution and geometry reduces the first error. Tight

coupling between the three modules must be achieved, with thin layers of ice accretion before airflow recalculation, to reduce the second error. Although this article does not show such results, this is currently achieved through the use of an efficient mesh displacement scheme.

Successful 3D calculations around slightly complex geometries have shown the capability of a second-generation computational fluid dynamics-based in-flight icing simulation system. Calculation around a 3D rotor blade tip has shown the capability of the code to calculate the flow field, droplet impingement and ice accretion all on the same mesh. A complete 3D ice accretion prediction on a Boeing 737-300 nacelle, whose flow solution and droplet impingement have already been successfully completed, has also

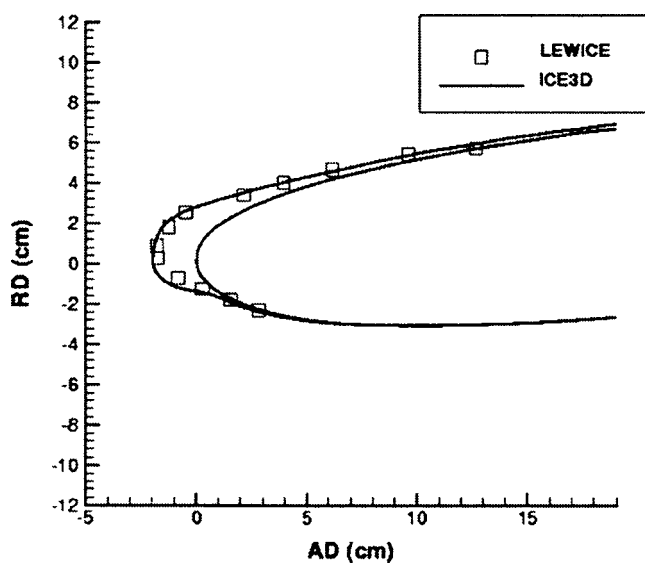


Fig. 19 Rime ice for the Boeing 737-300 inlet for 15 deg AoA, comparison of analytical ice shapes between ICE3D and LEWICE, circumferential cut at 135 deg

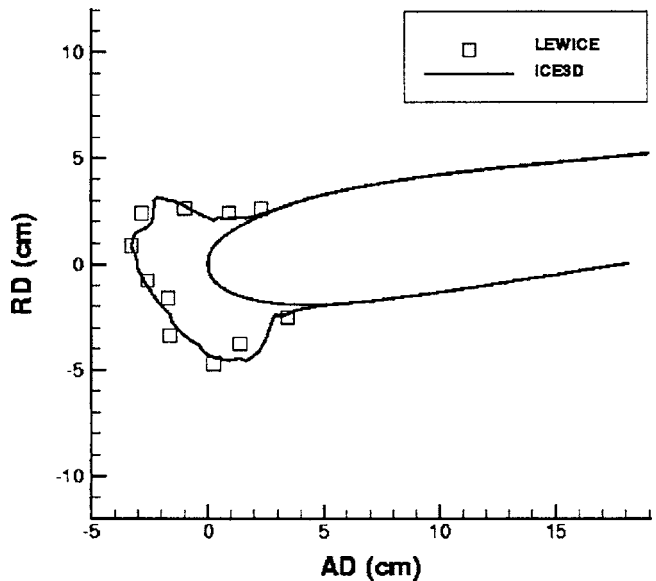


Fig. 21 Glaze ice for the Boeing 737-300 inlet for 15 deg AoA, comparison of analytical ice shapes between ICE3D and LEWICE, circumferential cut at 45 deg

been demonstrated. The code is now being used to tackle even more complex problems such as wing body junctions and high-lift wings.

Nomenclature

Airflow variables

- AOA = aerodynamic angle of attack
 h = heat transfer coefficient ($W/(m^2 K)$)
 L = characteristic length (m)
 P_∞ = pressure (Pa)
 \dot{Q}_h = convective heat flux (W)
 T_∞ = temperature at infinity (K)
 \mathbf{u}_a = air velocity (m/s)
 U_∞ = velocity at infinity (m/s)
 ρ_a = air density (kg/m^3)
 μ = laminar dynamic viscosity ($N s/m^2$)
 ν = laminar kinematic viscosity (m^2/s)
 τ_{wall} = air wall shear stress tensor (N/m^2)

Droplet variables

- d = droplet diameter (m)
 Fr = Froude number ($U_\infty / \sqrt{Lg_0}$)
 g_0 = magnitude of the gravity vector
 g = gravity vector (m/s^2)
 K = droplet inertia parameter ($\rho_w d^2 U_\infty / 18 L \mu_w$)
 LWC = liquid water content (g/m^3)
 Re_d = droplet Reynolds number ($d U_\infty (\mathbf{u}_a - \mathbf{u}_d) / \nu$)
 $\tilde{T}_{d,\infty}$ = droplets temperature at infinity ($^\circ C$)
 \mathbf{u}_d = droplets velocity (m/s)
 α = water volume fraction
 β = collection efficiency

Water, ice variables

- C_p = pressure coefficient
 C_{ice} = specific heat at constant pressure for ice ($J/(kg K)$)
 C_w = specific heat at constant pressure for water ($J/(kg K)$)
 h_f = film thickness (m)
 \dot{m}_{ice} = instantaneous mass of ice accretion (kg/s)
 \dot{m}_{evap} = instantaneous mass of evaporation (kg/s)
 L_{evap} = latent heat of evaporation (J/kg)
 L_{fusion} = latent heat of fusion at $0^\circ C$ (J/kg)
 L_{subl} = latent heat of sublimation (J/kg)
 T = temperature at wall / air / liquid-water / ice interface ($^\circ C$)
 t = time (s)
 $\mathbf{u}_f, \bar{\mathbf{u}}_f$ = film velocity vector and mean film velocity across the thickness (m/s)
 ϵ = solid emissivity
 σ = Boltzmann constant
 μ_w = dynamic viscosity of water ($N s/m^2$)
 ρ_w = water density (kg/m^3)

Geometric variables

- s = curvilinear distance from stagnation point
 $\mathbf{x}=(x_1, x_2)$ = coordinate along the wall
 y = coordinate normal to the wall
 X = rotor blade tip chordwise direction
 Y = rotor blade tip spanwise direction
 Z = normal direction to the plane (X, Y)

References

- [1] Messenger, B. L., 1953, "Equilibrium Temperature of an Unheated Icing Surface as a Function of Air Speed," *J. Aeronaut. Sci.*, **20**, pp. 29–42.
- [2] MacArthur, C. D., 1983, "Numerical Simulation of Airfoils Ice Accretion," AIAA Paper No. 83-0112.
- [3] Ruff, G. A., and Berkowitz, M., 1990, "Users Manual for the NASA Lewis Ice Accretion Prediction Code (LEWICE)," NASA Contractor Report No. 185129.
- [4] Hedde, T., and Guffond, D., 1995, "ONERA Three-Dimensional Icing Model," *AIAA J.*, **33**(6), pp. 1038–1045.
- [5] Gent, R. W., 1990, "TRAJICE2, A Combined Water Droplet and Ice Accretion Prediction Program for Aerofoil," DRA Technical Report No. TR90054.
- [6] Tran, P., Brahimi, M. T., and Paraschivoiu, I., 1994, "Ice Accretion on Aircraft Wings with Thermodynamic Effects," AIAA Paper No. 94-0605.
- [7] Bidwell, C., Pinella, D., and Garrison, P., 1999, "Ice Accretion Calculation for a Commercial Transport Using the LEWICE3D, ICEGRID3D and CMARC Programs," AIAA Paper No. 99-0250.
- [8] Baruzzi, G. S., Habashi, W. G., Guèvremont, G., and Hafez, M. M., 1995, "A Second Order Finite Element Method for the Solution of the Transonic Euler and Navier-Stokes Equations," *Int. J. Numer. Methods Fluids*, **20**, pp. 671–693.
- [9] Bourgault, Y., Habashi, W. G., Dompierre, J., and Baruzzi, G. S., 1999, "A Finite Element Method Study of Eulerian Droplets Impinging Models," *Int. J. Numer. Methods Fluids*, **29**, pp. 429–449.
- [10] Beaugendre, H., Morency, F., and Habashi, W. G., 2003, "FENSAP-ICE's Three-Dimensional In-flight Ice Accretion Module," *J. Aircr.*, **40**(2), pp. 239–247.
- [11] Croce, G., Beaugendre, H., and Habashi, W. G., 2002, "CHT3D: FENSAP-ICE Conjugate Heat Transfer Computations with Droplet Impingement and Runback Effects," AIAA Paper No. 2002-0386.
- [12] Spalart, P. R., and Allmaras, S. R., 1992, "A One-Equation Turbulence Model for Aerodynamic Flows," AIAA Paper No. 92-0439.
- [13] Spalart, P. R., 2000, "Trends in Turbulence Treatments," AIAA Paper No. 2000-2306.
- [14] Beaugendre, H., Morency, F., and Habashi, W. G., 2003, "Roughness Implementation in FENSAP-ICE: Model Calibration and Influence on Ice Shapes," *J. Aircr.*, **40**, pp. 1212–1215.
- [15] Beaugendre, H., 2003, "A PDE-Based 3D Approach for In-Flight Ice Accretion," Ph.D. dissertation, McGill University, Montreal, QC, Canada.
- [16] Habashi, W. G., Dompierre, J., Bourgault, Y., Fortin, M., and Vallet, M. -G., 1998, "Certifiable Computational Fluid Dynamics Through Mesh Optimization," Special Issue on Credible Computational Fluid Dynamics Simulation, *AIAA J.*, **36**(5), pp. 703–711.
- [17] Gresho, P. M., Lee, R. L., Sani, R. L., Maslanik, M. K., and Eaton, B. E., 1987, "The Consistent Galerkin FEM for Computing Derived Boundary Quantities in Thermal and/or Fluid Problems," *Int. J. Numer. Methods Fluids*, **7**, pp. 371–394.
- [18] Jackson, R., 2000, *The Dynamics of Fluidized Particles*, Cambridge University Press, Cambridge, Chap. 2.
- [19] Hughes, T. J. R., and Brooks, A., 1982, "A Theoretical Framework for Petrov-Galerkin Methods with Discontinuous Weighting Functions: Application to the Streamline-Upwind Procedure," *Finite Element in Fluids*, Gallagher, R. H., Norrie, D. H., Oden, J. T., and Zienkiewicz, O. C., eds., Wiley, New York, Vol. 4, Chap. 3.
- [20] Bourgault, Y., Beaugendre, H., and Habashi, W. G., 2000, "Development of a Shallow Water Icing Model in FENSAP-ICE," *J. Aircr.*, **37**, pp. 640–646.
- [21] Kays, W. M., and Crawford, B. M., 1993, *Convective Heat and Mass Transfer*, 3rd ed., McGraw-Hill, New York.
- [22] Wright, W. B., and Rutkowski, A., 1999, "Validation Results for LEWICE 2.0" and CD-ROM.
- [23] SAE Aerospace Recommended Practices, 2003, "Droplet Impingement and Ice Accretion Computer Codes," ARP5903.
- [24] Kind, R. J., "Ice Accretion Simulation Evaluation Test," NATO RTO Technical Report No. 38, RTO-TR-038, France, November, 2001.
- [25] Lepage, C. Y., Suerich-Gulick, F., and Habashi, W. G., 2002, "Anisotropic 3D Mesh Adaptation on Unstructured Hybrid Meshes," AIAA Paper No. 2002-0859.
- [26] Dompierre, J., Vallet, M. -G., Bourgault, Y., Fortin, M., and Habashi, W. G., 2002, "Anisotropic Mesh Adaptation: Towards User-Independent, Mesh-Independent and Solver-Independent CFD Solutions: Part III: Unstructured Meshes," *Int. J. Numer. Methods Fluids*, **39**, pp. 675–702.
- [27] Roache, P. J., 1998, *Verification and Validation in Computational Science and Engineering*, Hermosa, Albuquerque, New Mexico, Chap. 5.
- [28] Papadakis, M., Elangonan, R., Freund, G. A., Breer, J. M., Zumwalt, G. W., and Whitmer, L., 1989, "An Experimental Method for Measuring Water Droplet Impingement Efficiency on Two- and Three-Dimensional Bodies," NASA CR-4257, DOT/FAA/CT-87/22.
- [29] Bidwell, C. S., 1996, "Collection Efficiency and Ice Accretion Calculations for a Boeing 737-300 Inlet," SAE Paper No. 965570.
- [30] Tran, P., Benquet, P., Baruzzi, G., and Habashi, W. G., 2002, "Design of Ice Protection Systems and Icing Certification Through Cost-Effective Use of CFD," AIAA Paper No. 2002-0382.